Journal of Materials Chemistry A

ROYAL SOCIETY OF CHEMISTRY

PAPER

View Article Online
View Journal | View Issue

Open Access Article. Published on 20 3 2023. Downloaded on 2026-05-12 3:00:06.
This article is licensed under a Creative Commons Attribution-NonCommercial 3.0 Unported Licence.

Check for updates

Cite this: J. Mater. Chem. A, 2023, 11, 8912

# Enhanced thermoelectric performance in $Bi_{0.5}Sb_{1.5}Te_3$/SiC composites prepared by low-temperature liquid phase sintering†

Bo Zhu,[abe] Yi Luo,[a] Haiyi Wu,[a] Du Sun,[a] Luo Liu,[a] Shengcheng Shu,[c] Zhong-Zhen Luo,[d] Qiang Zhang,[*b] Ady Suwardi[*fg] and Yun Zheng[*a]

Amongst thermoelectrics, $Bi_2Te_3$ is special owing to its peak performance near room temperature, which enables it to be used for both energy harvesting and cooling. Despite extensive studies on this compound, $Bi_2Te_3$-based bulk materials are usually prepared by field-assisted sintering and hot pressing. This necessitates sophisticated equipment and tedious compositional control, both of which are undesirable for large scale applications. In this work, a low-temperature liquid phase sintering (LPS) method was employed to prepare p-type $Bi_{0.5}Sb_{1.5}Te_3$/SiC composites with enhanced thermoelectric properties. In addition, a nearly two-fold increase in the power factor was observed post heat treatment at 350 °C. This can be ascribed to carrier concentration modulation due to porosity induced by heat treatment. Further addition of 0.6 vol% SiC results in a low lattice thermal conductivity of 0.33 W $m^{-1}$ $K^{-1}$, which can be ascribed to phonon scattering due to various defects induced by the SiC inclusion. Ultimately, a figure of merit *ZT* of 1.05 at 340 K was achieved for $Bi_{0.5}Sb_{1.5}Te_3$/0.6 vol% SiC, 20% higher than that of the pristine sample. Moreover, an average *ZT* of 0.87 at 300–500 K was attained, comparable to state-of-the-art values *via* high-temperature processing. This work showcases the promising application of the low-temperature LPS technique for energy-efficient processing of thermoelectrics.

Received 19th December 2022
Accepted 20th March 2023

DOI: 10.1039/d2ta09850d

rsc.li/materials-a

## 1. Introduction

As a type of energy material that can convert thermal energy into electricity (and *vice versa*), thermoelectric materials have been used in space power generation, waste heat recycling, and thermoelectric refrigeration. They can also provide a fast time response for precise temperature control. In addition, they can realize frequent thermal cycling for polymerase chain reaction (PCR)-based testing, which is especially useful for diagnosing COVID-19.[1–6] Thermoelectric performance of materials can be characterized by the dimensionless figure of merit *ZT*, expressed as $ZT = \alpha^2\sigma T/(\kappa_L + \kappa_c)$, where $\alpha$, $\sigma$, $\kappa_c$, $\kappa_L$, and T represent the Seebeck coefficient, electrical conductivity, carrier thermal conductivity, lattice thermal conductivity, and absolute temperature, respectively.[7,8] The research of various thermoelectric materials has developed rapidly in the past century. Many state-of-the-art materials have emerged, including SnSe,[9,10] PbTe,[11,12] SiGe,[13,14] half-Heusler alloy,[15,16] skutterudite,[17,18] oxides[19] (such as $NaCo_2O_4$,[20,21] $CaMnO_3$,[22,23] ZnO,[24,25] and $SrTiO_3$,[26,27]), and Zintl.[28,29] Most of these materials are studied only in the laboratory and have a long way to go in terms of industrial production.[30]

Bismuth telluride-based materials have been commercialized for a wide range of applications. To date, it is the only mature material that has reasonably good performance for both cooling and low-grade heat harvesting. At present, high-temperature melting or zone melting is usually used to synthesize $(Bi,Sb)_2(Te,Se)_3$ thermoelectric materials.[31] The *ZT* value of either p-type or n-type is close to 1.0 at room temperature. However, traditional preparation methods take a long time, consume a lot of energy, and are not economical. Therefore, developing low temperature, low cost, high efficiency

[a]Key Laboratory of Optoelectronic Chemical Materials and Devices, Ministry of Education, Jianghan University, Wuhan 430056, China. E-mail: zhengyun@jhun.edu.cn

[b]Key Laboratory of Interface Science and Engineering in Advanced Materials, Ministry of Education, Taiyuan University of Technology, Taiyuan 030024, China. E-mail: zhangqiang@tyut.edu.cn

[c]Zhejiang Key Laboratory of Marine Materials and Protective Technologies, Ningbo Institute of Materials Technology and Engineering (NIMTE), Chinese Academy of Sciences, Ningbo 315201, China

[d]Key Laboratory of Eco-Materials Advanced Technology, College of Materials Science and Engineering, Fuzhou University, Fuzhou, 350108, China

[e]The Institute of Technological Sciences, Wuhan University, Wuhan 430072, China

[f]Institute of Materials Research and Engineering, Agency for Science, Technology and Research (A*STAR), Singapore 138634, Singapore. E-mail: ady_suwardi@imre.a-star.edu.sg

[g]Department of Materials Science and Engineering, National University of Singapore, Singapore 117575, Singapore

† Electronic supplementary information (ESI) available: See DOI: https://doi.org/10.1039/d2ta09850d



This journal is © The Royal Society of Chemistry 2023

Open Access Article. Published on 20 3 2023. Downloaded on 2026-05-12 3:00:06.
This article is licensed under a Creative Commons Attribution-NonCommercial 3.0 Unported Licence.

thermoelectric materials preparation methods has become a key challenge in thermoelectrics. So far, researchers have found many low-cost preparation methods on thermoelectric materials, such as the microwave method,[32,33] combustion synthesis reaction combined with the plasma activated sintering process,[34] and low-temperature liquid phase sintering (LPS) method.[35] Our earlier work using low-temperature LPS to prepare $Bi_2Te_3$-based materials has proven successful. But the obtained *ZT* values remain inferior compared to those obtained for existing materials used for commercial application.[35]

In this work, we present a strategy to drastically improve the thermoelectric performance of LPS-synthesized $Bi_2Te_3$-based materials. By low temperature heat treatment of LPS-synthesized $Bi_2Te_3$ samples combined with SiC nanoparticle (20 nm) inclusion, a high peak *ZT* of 1.05 at 340 K was achieved. This value is almost two times higher compared to the *ZT* of 0.56 at 450 K of LPS-synthesized $Bi_2Te_3$ reported previously. Such drastic improvements in the performance can partially be ascribed to the subsequent heat treatment, which is an efficient way to control lattice defects and carrier mobility.[36,37] Besides heat treatment, the inclusion of SiC nanoparticles further reduces the lattice thermal conductivity while retaining the electronic properties, further improving the *ZT*.[38–43] Furthermore, it was also evident from this work that small SiC nanoparticle dispersion in $(Bi,Sb)_2Te_3$ materials is more effective than large nanoparticles in improving its thermoelectric performance. Overall, the two key insights derived from this work can be widely applied to other materials systems. Firstly, LPS reported in this work represents both an energetically and commercially attractive alternative to high temperature processes in thermoelectric synthesis. Secondly, unlike chemical doping, nanocomposites using small nanoparticle inclusion (*i.e.* SiC) can be introduced to other materials systems without severely affecting their existing chemical configuration, which subsequently affects their band structures and transport properties.

## 2. Experimental section

### 2.1 Sample preparation

In this experiment, Bi shots (99.9%, Sichuan High Purity Material Technology Co., Ltd), Sb granules (99.8%, Sichuan High Purity Material Technology Co., Ltd) and Te chunks (99.9%, Sichuan High Purity Material Technology Co., Ltd) were used as raw materials. They were weighed according to the stoichiometry of $Bi_{0.5}Sb_{1.5}Te_3$ and loaded into a quartz tube. The quartz tube was then sealed under vacuum using vacuum sealing equipment (MRVS-2002, Partulab Technology Co. Ltd). The tube was then placed in a muffle furnace (VBF-1200X, Hefei Kejing Material Technology Co., Ltd) and heated to 800 °C (heating rate: 5 °C $min^{-1}$) for six hours and slowly cooled to room temperature. The ingots were crushed into powders using a high-energy mixer (8000M, SPEX SamplePrep, America). The ground powders were sieved using a 500-mesh stainless steel sieve. Then $Bi_{0.5}Sb_{1.5}Te_3$ powders and SiC nanoparticles with 20 nm in size were mixed by ball milling according to *x* vol% SiC/$Bi_{0.5}Sb_{1.5}Te_3$ ($x$ = 0, 0.1, 0.3, 0.6, 0.8, 1.0). The milling process was carried out in an argon atmosphere for 30 min. Seven-gram composite powders were weighed and blended with 1 mL deionized water to form a slurry. The slurry was consolidated into bulk materials using low temperature LPS as described in our previous work.[35] The specific sintering conditions are listed below: the sintering temperature is 150 °C, the applied pressure is 240 MPa, and the holding time is 20 min. The sintered cylinder samples were then loaded into a tube furnace (VBF-1200X, Hefei Kejing Material Technology Co., Ltd) for heat treatment under continuous argon purging. The heat treatment temperature was set at 200–400 °C in order to remove the residual water and promote crystallization. The schematic diagram of the synthesis flow is shown in Fig. S1.† The densities of all bulk materials were tested by the Archimedes method, and the samples were cut into rectangular strips ($12 \times 4 \times 2$ $mm^3$) and square pieces ($6 \times 6 \times 2$ $mm^3$) using a diamond saw (SYJ-400 Shenyang Kejing Auto-instrument Co., Ltd).

### 2.2 Testing and characterization

The crystal structure, grain orientation and phase composition of the bulk material were analyzed by X-ray diffraction (XRD, PANalytical X'Pert Power, Netherlands). Field emission scanning electron microscopy (FESEM, Hitachi SU8010, Japan) was used to characterize the grain microstructure and fracture morphology of the samples and was equipped with an energy dispersive spectrometer (EDS) to detect the composition. Samples were sectioned using a focused ion beam (FIB, TESCAN AMBER GMH Czech) and characterized by transmission electron microscopy (TEM, JEOL JEM ARM200F Nippon Electronics Co.). The fast Fourier transform (FFT) analysis of TEM images was performed using Gatan Digital Micrograph software. The Seebeck coefficient $\alpha$ and conductivity $\sigma$ were simultaneously measured using commercial equipment (MRS-3 Jouleyacht, China) in a temperature range of 300–500 K. $\alpha$ was measured by the dynamic method and $\sigma$ was measured by four-wire resistance measurement. The thermal diffusivity D was measured by laser flash analysis (LFA, Netzsch LFA-457, Germany). The thermal conductivity $\kappa$ is calculated according to the formula, $\kappa = DdC_P$ where the sample density $d$ is determined by the Archimedes method and the specific heat $C_P$ is measured using a differential scanning calorimeter and the three-line method (DSC, Netzsch DSC 200F3, Germany). The room temperature Hall coefficient of the sample was measured by van der Pauw's method (Jouleyacht HET, China), and the carrier concentration ($p$) and mobility ($\mu_H$) of the material were calculated accordingly.

## 3. Experimental results and discussion

The $Bi_{0.5}Sb_{1.5}Te_3$ samples heat-treated at 200–400 °C show consistent XRD patterns with that before heat treatment (Fig. S2†), well matching the reference pattern (JCPDS#49-1713). This reinforces the fact that there is no structural/phase change due to heat treatment. Fracture morphologies of $Bi_{0.5}Sb_{1.5}Te_3$ materials under different heat treatment conditions are shown in Fig. S3 and S4.† It is obvious that the pores on the material

Open Access Article. Published on 20 3 2023. Downloaded on 2026-05-12 3:00:06.
This article is licensed under a Creative Commons Attribution-NonCommercial 3.0 Unported Licence.

surface can be clearly seen and the porosity of the sample is getting higher and higher when the heat treatment temperature is 300–400 °C at the same magnification. This is mainly because swelling or volumetric expansion has appeared on the surface of the block sample after heat treatment at 350 °C and 400 °C (as shown in Fig. S5a†), which caused a reduction in the density of the bulk sample (as shown in Table 1 and Fig. S5b and c†) and an increase in porosity. In addition, this bright field TEM image reveals that small intergranular pores are present in the heat-treated samples (as shown in Fig. S5d and e†).[44–47] Meanwhile, abnormal grain growth occurs in the 250 °C treated sample compared to other samples. This indicates that the material is thermally activated (Ostwald ripening[48–52]) at this heat treatment temperature. Porosity and thermal activation between grains determine carrier mobility. These two factors play a competitive role in affecting carrier mobility. On the one hand, thermal activation (the grains are activated by heat treatment) reduces the interface area between the grains, which is conducive to the carrier transport process and increases the carrier mobility. Therefore, the carrier mobility begins to increase (in Table 1) when the heat treatment temperature is 250–300 °C. On the other hand, the porosity intensifies the scattering effect on the carriers, which reduces the carrier mobility. Therefore, carrier mobility shows a downward trend (Table 1). The effects of different heat treatment temperatures on the thermoelectric transport properties are shown in Fig. 1.

Table 1 Room-temperature density ($d$), electrical conductivity ($\sigma$), Seebeck coefficient ($\alpha$), Lorentz number ($L$), carrier effective mass ($m^*/m_0$, calculated according to the formula given in the literature[56]), carrier concentration ($p$), and carrier mobility ($\mu_H$) of heat-treated $Bi_{0.5}Sb_{1.5}Te_3$ samples

| Heat treatment temperature (°C) | $d$ (g cm$^{-3}$) | $\sigma$ (S cm$^{-1}$) | $\alpha$ (μV K$^{-1}$) | $L$ ($10^{-8}$ W Ω K$^{-2}$) | $m^*/m_0$ | $p$ ($10^{19}$ cm$^{-3}$) | $\mu_H$ (cm$^2$ V$^{-1}$ s$^{-1}$) |
|---|---|---|---|---|---|---|---|
| Without heat treatment | 6.62 | 398.6 | 153.6 | 1.72 | 1.13 | 4.38 | 80 |
| 200 | 6.55 | 451.3 | 146.1 | 1.70 | 1.01 | 4.11 | 69 |
| 250 | 6.55 | 409.6 | 159.0 | 1.68 | 1.01 | 3.88 | 65 |
| 300 | 5.92 | 430.1 | 211.7 | 1.67 | 0.92 | 1.52 | 176 |
| 350 | 5.58 | 547.7 | 204.4 | 1.62 | 0.84 | 1.53 | 282 |
| 400 | 5.30 | 483.4 | 205.1 | 1.61 | 0.98 | 1.92 | 192 |

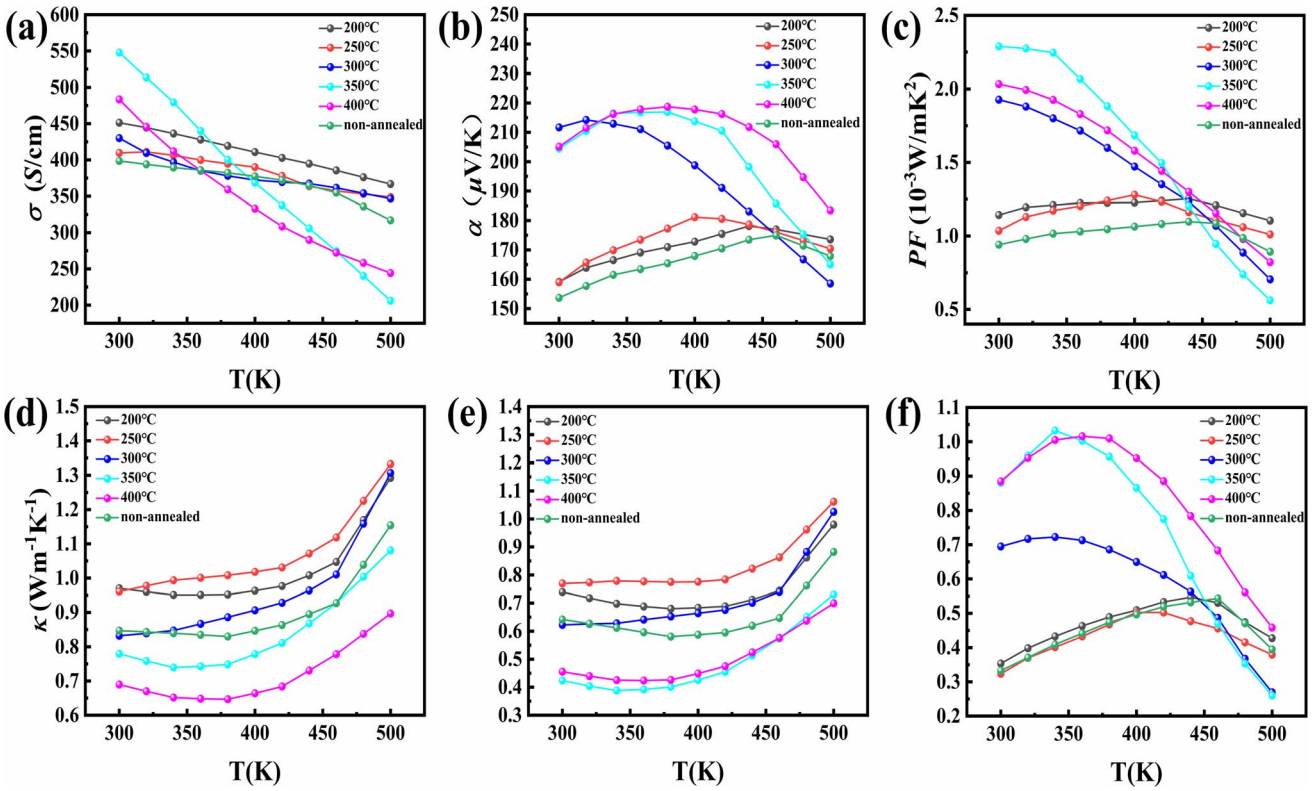


Fig. 1 Temperature-dependent thermoelectric properties of $Bi_{0.5}Sb_{1.5}Te_3$ materials under different heat treatment conditions: (a) electrical conductivity, (b) Seebeck coefficient, (c) power factor, (d) thermal conductivity, (e) the combined lattice and bipolar thermal conductivity, and (f) $ZT$ values.

Open Access Article. Published on 20 3 2023. Downloaded on 2026-05-12 3:00:06.
This article is licensed under a Creative Commons Attribution-NonCommercial 3.0 Unported Licence.

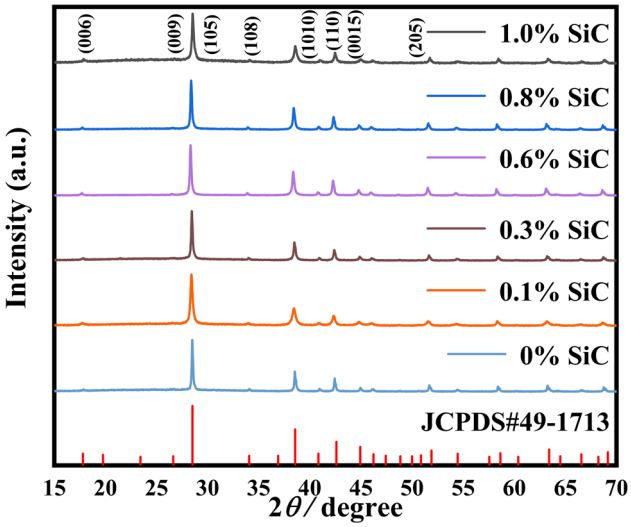


Fig. 2 XRD patterns of $Bi_{0.5}Sb_{1.5}Te_3$/$x$ vol% SiC ($x$ = 0, 0.1, 0.3, 0.6, 0.8, 1.0) pellet samples after heat treatment.

Fig. 1a shows the variation in the temperature dependent electrical conductivity of materials with different heat treatment temperatures. The room-temperature conductivity of the sample heat-treated at 350 °C is 547.73 S $cm^{-1}$, which is significantly higher than that of both the sample (398.55 S $cm^{-1}$) without heat treatment and the 200 °C heat-treated sample (451.29 S $cm^{-1}$). This is mainly due to its more than three times higher room temperature carrier mobility compared to that of the sample without heat treatment (as shown in Table 1). As shown in Fig. 1b, the samples heat-treated at 350 °C and 400 °C show much higher Seebeck coefficients than that before heat treatment. This is mainly because the carrier concentration is greatly reduced by heat treatment at 350 °C and 400 °C (as shown in Table 1). The decreased carrier concentration could be ascribed to strengthened carrier scattering at the pores induced by heat treatment.[44,46,53,54] Moreover, the intrinsic excitation temperature of samples heat-treated at 350 °C and 400 °C is shifted to around 360 K. The power factor of the samples heat-treated at 350 °C and 400 °C is much higher than that of the sample without heat treatment and 200 °C samples prior to the intrinsic excitation (as shown in Fig. 1c). Fig. 1d shows the temperature dependent thermal conductivities of heat-treated materials. Obviously, the thermal conductivity of samples heat-treated at 350 °C and 400 °C is significantly lower than that of the sample without heat treatment and the heat-treated samples at 200 °C with regard to 350 °C. Fig. 1e shows the variation of the combined lattice and bipolar thermal conductivity $\kappa - \kappa_e$ (which can be calculated by a subtraction of the electronic contribution according to the formula $\kappa_L + \kappa_b = \kappa - \kappa_e$ and $\kappa_e = L\sigma T$)with different heat treatment temperatures as a function of temperature. It is significantly lower than that of the sample without heat treatment and heat-treated samples at 200 °C. The minimum combined lattice and bipolar thermal conductivity of the samples heat-treated at 350 °C reaches 0.38 W $m^{-1}$ $K^{-1}$ at 340 K (lower than the reference value[55]). Fig. 1f shows the temperature dependent $ZT$ of samples heat-treated at different temperatures. Obviously, the samples heat-treated at

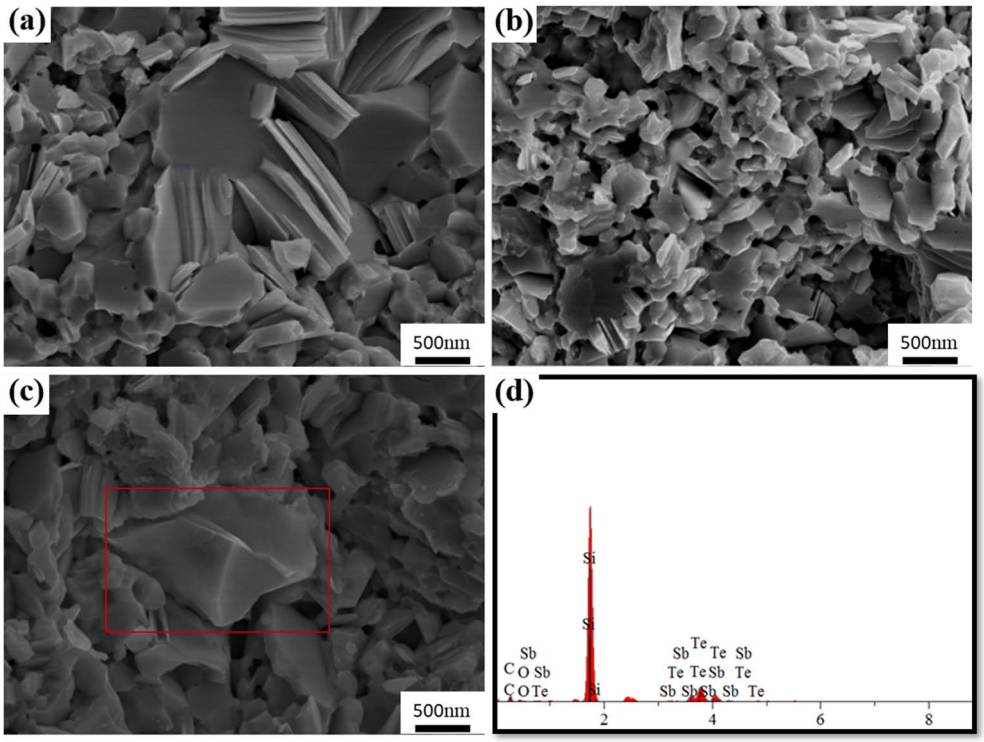


Fig. 3 Fracture morphologies and EDS compositions of $Bi_{0.5}Sb_{1.5}Te_3$/$x$vol% SiC ($x$ = 0, 0.6) bulk samples. Fracture morphologies of (a) $x$ = 0 and (b) and (c) $x$ = 0.6 samples; (d) EDS composition of the rectangular area in (c).

Open Access Article. Published on 20 3 2023. Downloaded on 2026-05-12 3:00:06.
This article is licensed under a Creative Commons Attribution-NonCommercial 3.0 Unported Licence.

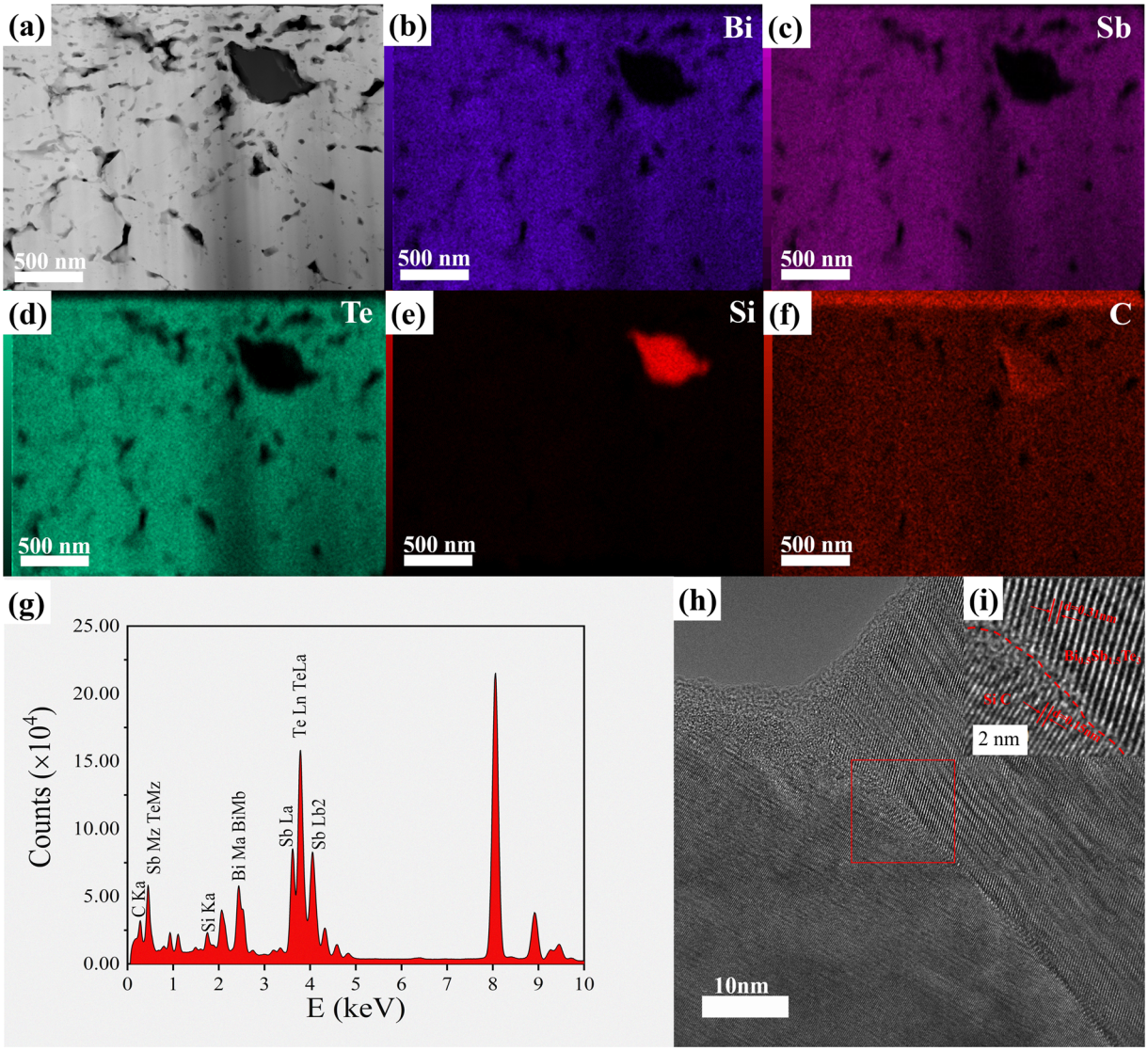


Fig. 4 (a) The microstructure of $Bi_{0.5}Sb_{1.5}Te_3$/*x*vol% SiC ($x = 0.6$), (b–f) the distribution of Si, Bi, Sb and Te elements, (g) EDS composition of $Bi_{0.5}Sb_{1.5}Te_3$/*x*vol% SiC ($x = 0.6$), (h) high-resolution TEM images of $x = 0.6$ samples, and (i) high-resolution TEM images of $x = 0.6$ sample interfaces ((i) is the image of the red rectangular area in (h)).

350 °C or 400 °C have higher *ZT* values, reaching a peak value of ~1.0 near 350 K. The average *ZT* values are around 0.75–0.85 for samples heat-treated at 350 and 400 °C (Fig. S6†). In summary, the optimal heat treatment temperature of low-temperature liquid phase sintered samples is within the range of 350–400 °C. It should be noted that samples heat-treated at 400 °C have poor machinability, leading to sample fracture during the cutting process and difficulty in the thermoelectric performance test. Therefore, the samples were heat-treated at 350 °C in the subsequent experiments.

Fig. 2 shows the phase composition of $Bi_{0.5}Sb_{1.5}Te_3$/SiC composite samples. All the XRD peaks of the samples correspond to the reference $Bi_{0.5}Sb_{1.5}Te_3$ (JCPDS#49–1713). No additional peaks related to SiC and impurities were observed within the XRD detection limit, consistent with the minute amount of SiC. Fig. 3 presents the fracture morphology and composition of $Bi_{0.5}Sb_{1.5}Te_3$/*x* vol% SiC ($x = 0$, 0.6) samples. Many lamellar crystals were observed in the cross section (Fig. 3a and b), which are expected in the layered structure of $Bi_2Te_3$-based compounds. Compared with the pristine sample, the 0.6 vol% SiC incorporated composite sample has smaller grains. This indicates that introducing SiC nanoparticles can effectively inhibit grain growth, consistent with previous reports.[57] Fig. 3d shows the EDS composition map of the red rectangular region in Fig. 3c where obvious Si signals were detected, indicative of the SiC existence as a separate phase. Meanwhile, EDS mapping and quantitative results of $Bi_{0.5}Sb_{1.5}Te_3$/*x* vol% SiC ($x = 0.6$) sample at low magnitude (as shown in Fig. S7 and S8†). It is obvious that silicon carbide has good dispersion in the bismuth telluride matrix and the atomic ratio is also within the normal error range.

To further characterize the microstructure, transmission electron microscopy (TEM) was used to detect the defects in the crystal, such as dislocations and lattice distortion. Fig. S9a and c†

 This journal is © The Royal Society of Chemistry 2023

Open Access Article. Published on 20 3 2023. Downloaded on 2026-05-12 3:00:06.
This article is licensed under a Creative Commons Attribution-NonCommercial 3.0 Unported Licence.

show high-resolution TEM images of $x = 0$ and $x = 0.6$ samples, respectively. Evidently, Fig. S9a† shows atomic-scale dislocations and lattice distortions. Meanwhile, the inverse FFT images in Fig. S9b and d† show the dislocations and lattice distortions in the (018) for $x = 0$ and the (015) for $x = 0.6$ crystal planes, respectively. In addition, similar defects are observed in other regions of Fig. S9a and c.† These specific microstructures and defects, including high concentrations of grain boundaries, dislocations and lattice distortions, have a significant impact on electrical and thermal transport properties. These defects play an important role in inducing phonon scattering and designing low lattice thermal conductivity. Fig. 4a presents the low-magnification TEM image together with the mapping and EDS results (Fig. 4b–g) showing the SiC particles distributed in the $(Bi,Sb)_2Te_3$ matrix. The results in Fig. 4b–g show that silicon carbide has good dispersion in the BST matrix and also indicate that the $Bi_{0.5}Sb_{1.5}Te_3$/$x$vol% SiC composite has been successfully prepared Meanwhile, clear interfaces are formed between p-type $(Bi,Sb)_2Te_3$ (as shown in Fig. 4h and i) and SiC due to their similar lattice constants which is the prerequisite for generating the energy-filtering effect.[58,59]

Fig. 5 shows the temperature dependent electrical and thermal transport properties of $Bi_{0.5}Sb_{1.5}Te_3$/$x$ vol% SiC ($x = 0$, 0.1, 0.3, 0.6, 0.8, and 1.0). The SiC incorporation decreases the

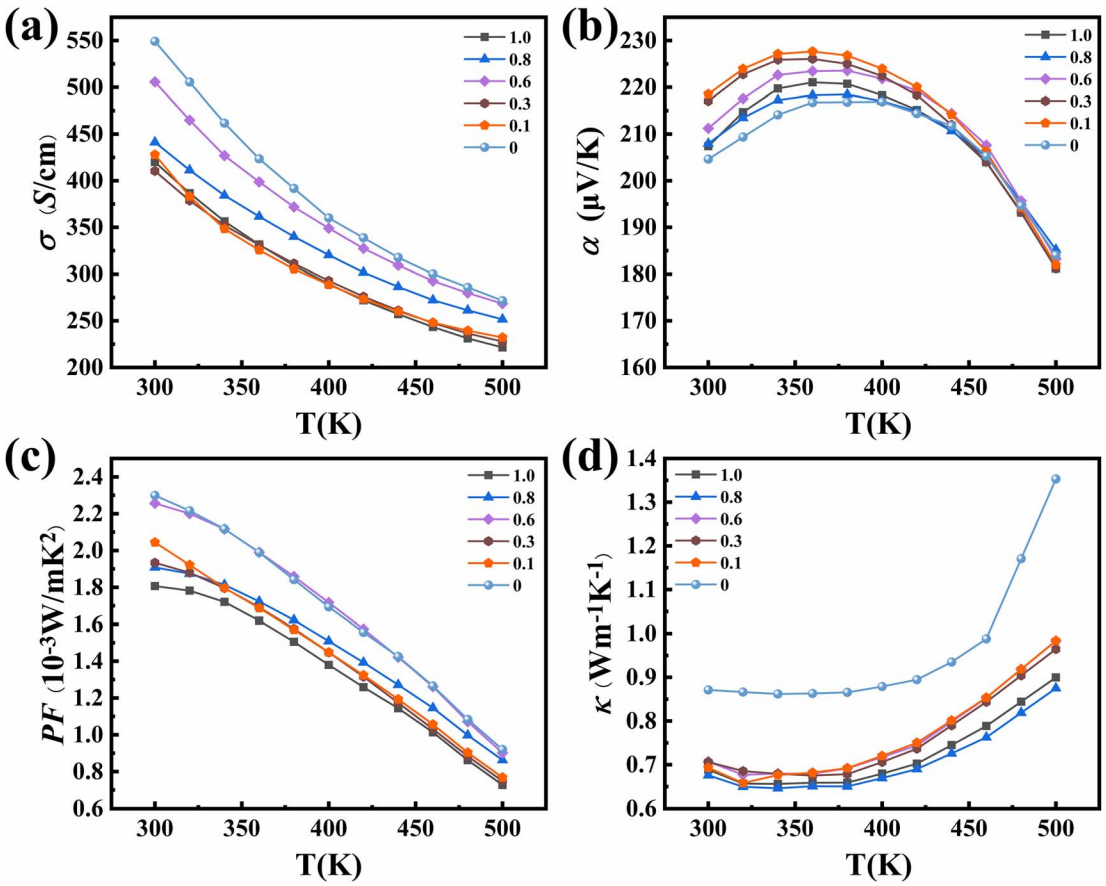


Fig. 5 (a) Electrical conductivity, (b) Seebeck coefficient, (c) power factor, and (d) thermal conductivity of $Bi_{0.5}Sb_{1.5}Te_3$/$x$ vol% SiC ($x = 0$, 0.1, 0.3, 0.6, 0.8, 1.0) as a function of temperature.

Table 2 Density ($d$), electrical conductivity ($\sigma$), Seebeck coefficient ($\alpha$), Lorentz ($L$), effective mass ($m^*/m_0$, calculated according to the formula given in the literature[56]), carrier concentration ($p$), and carrier mobility ($\mu_H$) of $Bi_{0.5}Sb_{1.5}Te_3$/SiC composites at room temperature

| $x$vol% SiC | $d$ (g cm$^{-3}$) | $\sigma$ (S cm$^{-1}$) | $\alpha$ (μV K$^{-1}$) | $L$ ($10^{-8}$ W Ω K$^{-2}$) | $m^*/m_0$ | $p$ ($10^{19}$ cm$^{-3}$) | $\mu_H$ (cm$^2$ V$^{-1}$ s$^{-1}$) |
|---|---|---|---|---|---|---|---|
| 0 | 5.58 | 547.7 | 204.6 | 1.62 | 0.87 | 1.53 | 224 |
| 0.1 | 5.73 | 427.9 | 218.6 | 1.60 | 0.98 | 1.55 | 173 |
| 0.3 | 5.75 | 410.4 | 217.0 | 1.60 | 1.01 | 1.65 | 155 |
| 0.6 | 5.80 | 505.7 | 211.2 | 1.61 | 0.95 | 1.60 | 199 |
| 0.8 | 5.66 | 441.2 | 207.9 | 1.61 | 0.85 | 1.42 | 199 |
| 1.0 | 5.43 | 420.0 | 207.4 | 1.61 | 0.90 | 1.56 | 168 |

Open Access Article. Published on 20 3 2023. Downloaded on 2026-05-12 3:00:06.
This article is licensed under a Creative Commons Attribution-NonCommercial 3.0 Unported Licence.

carrier mobility of $Bi_{0.5}Sb_{1.5}Te_3$-based materials. For example, the carrier mobilities of the $x = 0$ and 0.6 samples are 224 $cm^2$ $V^{-1}s^{-1}$ and 199 $cm^2$ $V^{-1}s^{-1}$, respectively (Table 2). When the content of silicon carbide ($x$ < 0.6%) gradually increases, the mutual scattering between carriers caused by an increase in the carrier concentration will greatly reduce the carrier mobility. When the silicon carbide content ($x \geq$ 0.6%) continues to increase, the second phase scattering strengthens, which decreases the carrier concentration and increases carrier mobility. In addition, for $x = 0$ and 0.6 samples, their electrical conductivities reach above 500 S $cm^{-1}$ at 300 K as shown in Fig. 5a, higher than those of the other composite samples. Fig. 5b shows the Seebeck coefficients of all samples as a function of temperature. The Seebeck coefficients of all samples increased with the increasing temperature, peaking at around 350 K and decreasing gradually. This is attributed to the intrinsic excitation occurring at above 350 K. The $x = 0.6$ sample exhibits a higher Seebeck coefficient (218.6 μV $K^{-1}$) than that without SiC (204.6 μV $K^{-1}$) despite their similar carrier concentrations, indicating the possible energy filtering effect induced by a small amount of SiC nanoparticles.[40] The energy barriers can filter low-energy carriers, which could increase Seebeck coefficients of the samples.[43] The enhanced Seebeck coefficient compensates for decreased electrical conductivity, resulting in a large power factor of $2.25 \times 10^{-3}$ W $mK^{-1}$ (ref. 2) at 300 K for the $x = 0.6$ sample. This is the highest value among all samples, nearly unchanged compared to pristine $Bi_{0.5}Sb_{1.5}Te_3$ (Fig. 5c) despite the lower thermal conductivity. The temperature dependent thermal conductivities of samples with different SiC contents are shown in Fig. 5d. Compared to the pristine sample, all SiC-containing samples show much smaller thermal conductivities in the entire temperature range. The thermal conductivities decrease slowly, reach the minimum value at around 350 K and increase with increasing temperature. This manifests the effective role of SiC inclusion in reducing the total thermal conductivity of $Bi_{0.5}Sb_{1.5}Te_3$.

Fig. 6a shows the combined lattice and bipolar thermal conductivity (as shown in Fig. S10,† it was calculated according to the formula given in the literature[60]) $\kappa - \kappa_e$ (which can be calculated by a subtraction of the electronic contribution according to the formula $\kappa - \kappa_e = \kappa_L + \kappa_b$ and $\kappa_e = L\sigma T$) of samples with different SiC contents as a function of temperature. As the temperature increases, the combined lattice and bipolar thermal conductivity gradually increases (due to bipolar diffusion). The lattice conductivities of all SiC-incorporated samples maintain the same trend (as shown in Fig. 6b), which presents a steady decrease followed by a gradual increase with increasing temperature. Compared to the other samples, the $x = 0.6$ sample has the lowest room-temperature lattice conductivity of 0.33 W $m^{-1}$ $K^{-1}$, much lower than that of the pristine

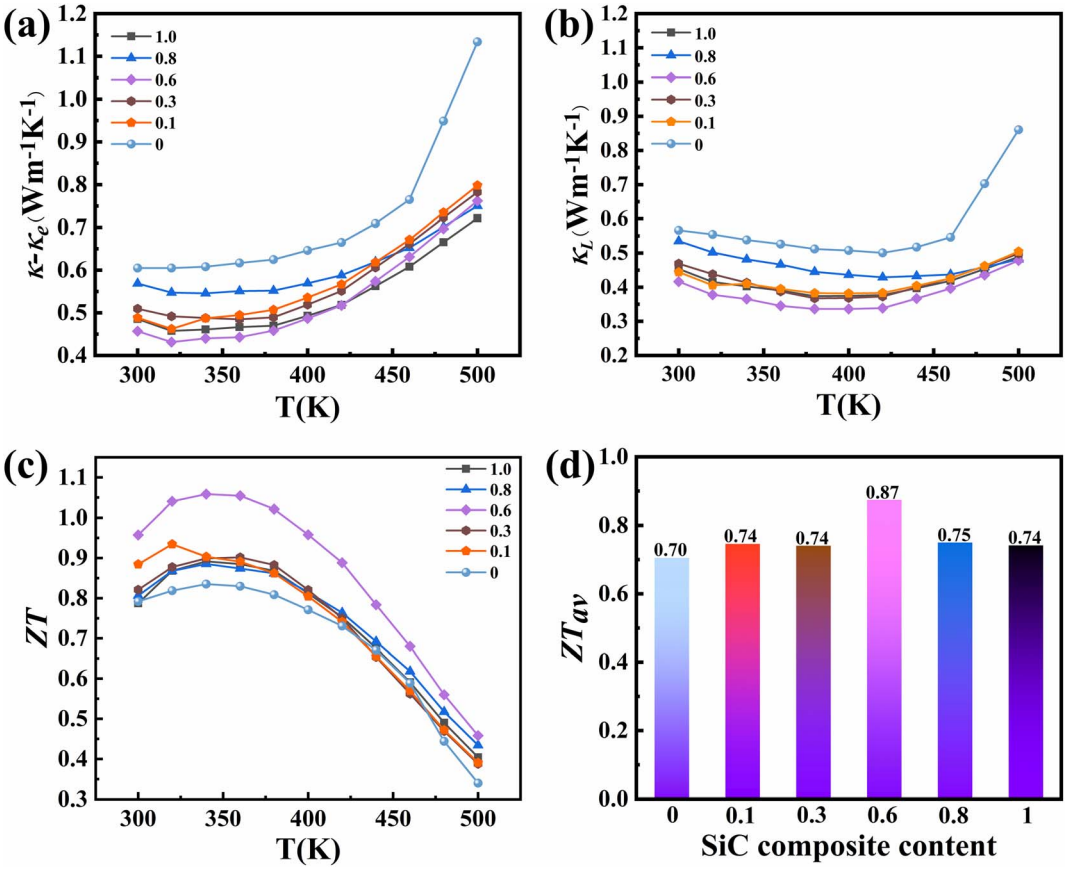


Fig. 6 (a) The combined lattice and bipolar thermal conductivity, (b) lattice thermal conductivity, and (c) $ZT$ values as a function of temperature for $Bi_{0.5}Sb_{1.5}Te_3$/$x$ vol% SiC ($x$ = 0, 0.1, 0.3, 0.6, 0.8, and 1.0) composite samples. (d) Average $ZT$ values at 300–500 K for the composites.

Open Access Article. Published on 20 3 2023. Downloaded on 2026-05-12 3:00:06.
This article is licensed under a Creative Commons Attribution-NonCommercial 3.0 Unported Licence.

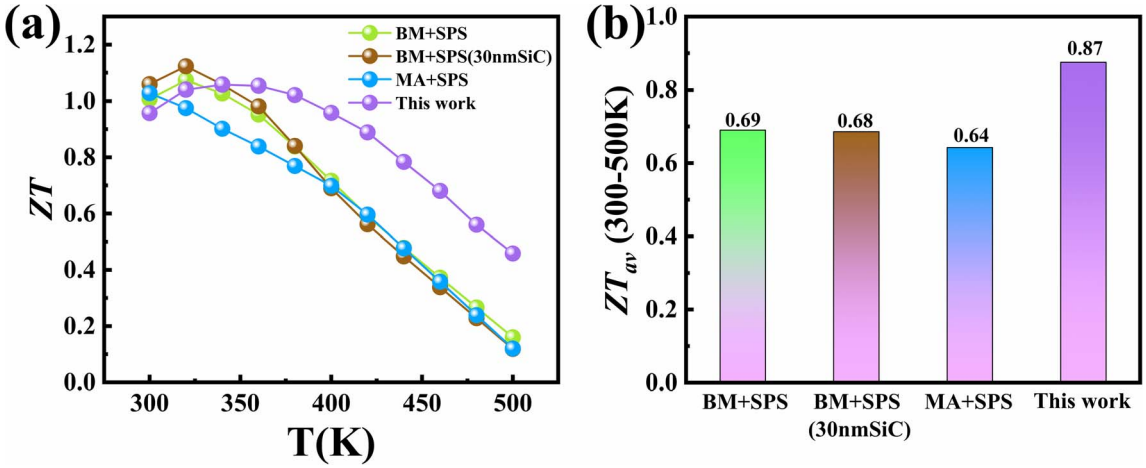


Fig. 7 Comparison of (a) temperature dependent *ZT* values and (b) $ZT_{av}$ for $Bi_{0.5}Sb_{1.5}Te_3$/SiC composites prepared by different methods.

sample. This is mainly ascribed to the enhanced phonon scattering by multiple scattering centers, including pores, grain boundaries, phase boundaries, dislocations and lattice distortions (as described above).[44,61–64] Specifically, the low-temperature LPS method can inhibit grain growth to obtain ultra-fine grains.[35] And after heat treatment at 350 °C, all samples demonstrate decreased density and improved porosity, leading to additional phonon scattering at the pores. A simplified Debye-Callaway model accounting for contributions from the grain boundaries, point defects, and SiC nanoparticles is shown in Fig. S11.† The fitting parameters were taken from ref. [65]. From the modelled lattice thermal conductivity, it is evident that when 0.6% SiC is added to the matrix, further reduction in lattice thermal conductivity can be observed. At higher temperatures (above 400 K), the upturn in experimental lattice thermal conductivity can be ascribed to deviation in the bipolar and electronic thermal conductivity estimation. This supports the premise that lattice thermal conductivities are reduced in SiC-incorporated samples. Fig. 6c shows the temperature dependent *ZT* values of the composite samples. The $x = 0.6$ sample exhibits the highest *ZT* value over the whole temperature range among all samples, achieving a peak value of 1.05 near 340 K. This is comparable to other samples prepared by field-assisted sintering or hot pressing.[5,66–68] In addition, the average *ZT* value of the $x = 0.6$ sample at 300–500 K is 0.87 (Fig. 6d), which is the highest among all samples and close to the literature value.[69]

In addition, in order to further reveal the advantages of low-temperature LPS, we compared the thermoelectric properties of $Bi_{0.5}Sb_{1.5}Te_3/x$ vol% SiC composite specimens prepared by mechanical alloying (ball milling) and spark plasma sintering (MA-SPS or BM-SPS) (Fig. 7).[39,57,70] Despite having a lower peak *ZT* value compared to SPS samples (Fig. 7a), the LPS samples show a higher average *ZT* value (Fig. 7b). Compared to consolidation methods, such as SPS and hot pressing, the low-temperature LPS method is low-temperature and is cost-efficient, making it conducive to large-scale industrial production. Furthermore, this study offers follow-up optimization possibilities. (1) It is important to control the Bi/Sb ratio to achieve the optimum hole concentration, thereby enhancing *ZT* values in $(Bi,Sb)_2Te_3$-based materials.[40,70–73] (2) Excess Te could be involved in $(Bi,Sb)_2Te_{3+x}$, which can reduce lattice thermal conductivity and improve carrier mobility.[44,74,75] (3) Other alternative secondary inorganic phases (such as carbon nanotubes,[76] $FeTe_2$ (ref. 77) and $Al_2O_3$ (ref. [68]) and conducting polymers can be considered.

## 4. Conclusions and outlook

This work adopted a novel low-temperature LPS and a subsequent heat treatment process to prepare $Bi_{0.5}Sb_{1.5}Te_3$/SiC composite specimens with enhanced thermoelectric properties. The results show that the additional heat treatment process at 350–400 °C is essential to boost the power factor of the as-sintered samples. Further improvements in the thermoelectric properties can be achieved by introducing a small amount of SiC nanoparticles in $Bi_{0.5}Sb_{1.5}Te_3$. The SiC addition combined with suppressed grain growth and other crystal defects results in enhanced phonon scattering. The lattice thermal conductivity of the 0.6 vol% SiC composite sample is as low as 0.33 W $m^{-1}$ $K^{-1}$ near 340 K, contributing to a maximum *ZT* value of 1.05 at 340 K, comparable to the literature reports. Meanwhile, the average *ZT* value of this sample reached 0.87, 24% higher than that of the pristine sample. This study proves the promising role of the low-temperature LPS method in preparing $(Bi,Sb)_2(Te,Se)_3$ bulk materials with drastically enhanced thermoelectric performance.

## Conflicts of interest

The authors declare no competing financial interest.

## Acknowledgements

Y. Z. would like to acknowledge financial support from the National Natural Science Foundation of China (Grant No.

Open Access Article. Published on 20 3 2023. Downloaded on 2026-05-12 3:00:06.
This article is licensed under a Creative Commons Attribution-NonCommercial 3.0 Unported Licence.

52102257) and Knowledge Innovation Program of the Wuhan-Shuguang Project (Grant No. 2022010801020375). A.S. acknowledges funding from A*STAR (Agency of Science, Technology and Research) Career Development Fund (CDF) no. C210112022.

## References

1 J. Ding, W. Zhao, W. Jin, C.-A. Di and D. Zhu, *Adv. Funct. Mater.*, 2021, **31**, 2010695.
2 Z. Soleimani, S. Zoras, B. Ceranic, Y. Cui and S. Shahzad, *Nano Energy*, 2021, **89**, 106325.
3 B. Qin, D. Wang, X. Liu, Y. Qin, J.-F. Dong, J. Luo, J.-W. Li, W. Liu, G. Tan, X. Tang, J.-F. Li, J. He and L.-D. Zhao, *Science*, 2021, **373**, 556–561.
4 J. Recatala-Gomez, A. Suwardi, I. Nandhakumar, A. Abutaha and K. Hippalgaonkar, *ACS Appl. Energy Mater.*, 2020, **3**, 2240–2257.
5 J. Wei, L. Yang, Z. Ma, P. Song, M. Zhang, J. Ma, F. Yang and X. Wang, *J. Mater. Sci.*, 2020, **55**, 12642–12704.
6 H. Alam and S. Ramakrishna, *Nano Energy*, 2013, **2**, 190–212.
7 Y. Zheng, T. J. Slade, L. Hu, X. Y. Tan, Y. Luo, Z.-Z. Luo, J. Xu, Q. Yan and M. G. Kanatzidis, *Chem. Soc. Rev.*, 2021, **50**, 9022–9054.
8 X. Yang, C. Wang, R. Lu, Y. Shen, H. Zhao, J. Li, R. Li, L. Zhang, H. Chen, T. Zhang and X. Zheng, *Nano Energy*, 2022, **101**, 107553.
9 A. Banik and K. Biswas, *Joule*, 2019, **3**, 636–638.
10 Z.-G. Chen, X. Shi, L.-D. Zhao and J. Zou, *Prog. Mater. Sci.*, 2018, **97**, 283–346.
11 C. Wang, X. Zhao, S. Ning, Q. Tao, Y. Tang, Z. Chen, J. Wu, X. Su and X. Tang, *Mater. Today Energy*, 2022, **25**, 100962.
12 B. Jia, Y. Huang, Y. Wang, Y. Zhou, X. Zhao, S. Ning, X. Xu, P. Lin, Z. Chen, B. Jiang and J. He, *Energy Environ. Sci.*, 2022, **15**, 1920–1929.
13 I. Donmez Noyan, G. Gadea, M. Salleras, M. Pacios, C. Calaza, A. Stranz, M. Dolcet, A. Morata, A. Tarancon and L. Fonseca, *Nano Energy*, 2019, **57**, 492–499.
14 K. Xie and M. C. Gupta, *J. Alloys Compd.*, 2020, **820**, 153182.
15 M. Mitra, A. Benton, M. S. Akhanda, J. Qi, M. Zebarjadi, D. J. Singh and S. J. Poon, *Mater. Today Phys.*, 2022, **28**, 100900.
16 M. M. Mallick and S. Vitta, *J. Mater. Chem. A*, 2018, **6**, 14709–14716.
17 Z.-Y. Liu, J.-L. Zhu, X. Tong, S. Niu and W.-Y. Zhao, *J. Adv. Ceram.*, 2020, **9**, 647–673.
18 S. El Oualid, I. Kogut, M. Benyahia, E. Geczi, U. Kruck, F. Kosior, P. Masschelein, C. Candolfi, A. Dauscher, J. D. Koenig, A. Jacquot, T. Caillat, E. Alleno and B. Lenoir, *Adv. Energy Mater.*, 2021, **11**, 2100580.
19 Y. Yin, B. Tudu and A. Tiwari, *Vacuum*, 2017, **146**, 356–374.
20 Y. A. Shah, M. J. Iqbal, K. Rasool, A.-u.-R. Makhdoom, Y. Iqbal, A. Ullah and M. Habib, *Appl. Phys. A: Solids Surf.*, 2020, **126**, 376.
21 E. M. Jakubczyk, A. Mapp, C. C. Chung, C. L. Sansom, J. L. Jones and R. A. Dorey, *J. Alloys Compd.*, 2019, **788**, 91–101.
22 T. Chen, J. Wang, X. Wang, H. Wang, W. Su, J. Zhai, F. Mehmood, M. Khan and C. Wang, *Appl. Mater. Today*, 2022, **29**, 101557.
23 Z. Shi, S. Tong, J. Wei, Y. Guo, Y. Zhang, L. Wang and J. Zhang, *ACS Appl. Mater. Interfaces*, 2022, **14**, 32166–32175.
24 S. Sulaiman, S. Izman, M. B. Uday and M. F. Omar, *RSC Adv.*, 2022, **12**, 5428–5438.
25 W. Lee, S. Lee, H. Kim and Y. Kim, *Chem. Eng. J.*, 2021, **415**, 128935.
26 X.-L. Shi, H. Wu, Q. Liu, W. Zhou, S. Lu, Z. Shao, M. Dargusch and Z.-G. Chen, *Nano Energy*, 2020, **78**, 105195.
27 Q.-Q. Fu, H. Gu, J.-J. Xing, Z. Cao and J. Wang, *Acta Mater.*, 2022, **229**, 117785.
28 N. Tomitaka, Y. Goto, K. Morino, K. Hoshi, Y. Nakahira, H. Ito, A. Miura, H. Usui and Y. Mizuguchi, *J. Mater. Chem. A*, 2021, **9**, 26362–26370.
29 L. Borgsmiller and G. J. Snyder, *J. Mater. Chem. A*, 2022, **10**, 15127–15135.
30 Z.-Z. Luo, S. Cai, S. Hao, T. P. Bailey, H. Xie, T. J. Slade, Y. Liu, Y. Luo, Z. Chen, J. Xu, W. Luo, Y. Yu, C. Uher, C. Wolverton, V. P. Dravid, Z. Zou, Q. Yan and M. G. Kanatzidis, *J. Am. Chem. Soc.*, 2022, **144**, 7402–7413.
31 Y. Zheng, X. Y. Tan, X. Wan, X. Cheng, Z. Liu and Q. Yan, *ACS Applied Energy Materials*, 2020, **3**, 2078–2089.
32 C. S. Birkel, W. G. Zeier, J. E. Douglas, B. R. Lettiere, C. E. Mills, G. Seward, A. Birkel, M. L. Snedaker, Y. Zhang, G. J. Snyder, T. M. Pollock, R. Seshadri and G. D. Stucky, *Chem. Mater.*, 2012, **24**, 2558–2565.
33 L. Wang, R. Zhang, L. Bo, F. Li, Y. Hou, M. Zuo and D. Zhao, *JOM*, 2022, **74**, 4250–4257.
34 G. Zheng, X. Su, T. Liang, Q. Lu, Y. Yan, C. Uher and X. Tang, *J. Mater. Chem. A*, 2015, **3**, 6603–6613.
35 B. Zhu, X. Su, S. Shu, Y. Luo, X. Y. Tan, J. Sun, D. Sun, H. Zhang, Q. Zhang, A. Suwardi and Y. Zheng, *ACS Applied Energy Materials*, 2022, **5**, 2002–2010.
36 Z.-L. Wang, T. Araki, T. Onda and Z.-C. Chen, *J. Mater. Sci.*, 2018, **53**, 9117–9130.
37 J. Li, C. Zhang, Y. Feng, C. Zhang, Y. Li, L. Hu, W. Ao and F. Liu, *J. Alloys Compd.*, 2019, **808**, 151747.
38 H. Liu, Z. Guo, X. Duan, X. Yuan and Q. Gao, *J. Electron. Mater.*, 2022, **51**, 516–521.
39 B. Cai, J. Pei, J. Dong, H.-L. Zhuang, J. Gu, Q. Cao, H. Hu, Z. Lin and J.-F. Li, *Sci. China Mater.*, 2021, **64**, 2551–2562.
40 D. Zhang, J. Lei, W. Guan, Z. Ma, C. Wang, L. Zhang, Z. Cheng and Y. Wang, *J. Alloys Compd.*, 2019, **784**, 1276–1283.
41 Y. Pan, U. Aydemir, F.-H. Sun, C.-F. Wu, T. C. Chasapis, G. J. Snyder and J.-F. Li, *Adv. Sci.*, 2017, **4**, 1700259.
42 M. G. Kanatzidis, *Chem. Mater.*, 2010, **22**, 648–659.
43 M. S. Dresselhaus, G. Chen, M. Y. Tang, R. G. Yang, H. Lee, D. Z. Wang, Z. F. Ren, J. P. Fleurial and P. Gogna, *Adv. Mater.*, 2007, **19**, 1043–1053.
44 I. T. Witting, J. A. Grovogui, V. P. Dravid and G. J. Snyder, *J. Materiomics*, 2020, **6**, 532–544.
45 T. Hamachiyo, M. Ashida and K. Hasezaki, *J. Electron. Mater.*, 2009, **38**, 1048–1051.

 This journal is © The Royal Society of Chemistry 2023

Open Access Article. Published on 20 3 2023. Downloaded on 2026-05-12 3:00:06.
This article is licensed under a Creative Commons Attribution-NonCommercial 3.0 Unported Licence.

46 C. C. Zhang, X. A. Fan, J. Hu, C. P. Jiang, B. Feng, Q. S. Xiang, G. Q. Li and Y. W. Li, *Adv. Eng. Mater.*, 2016, **18**, 1777–1784.
47 K. Zhao, H. Duan, N. Raghavendra, P. Qiu, Y. Zeng, W. Zhang, J. Yang, X. Shi and L. Chen, *Adv. Mater.*, 2017, **29**, 1701148.
48 Q. Liu, Q. Liu, Y. Wu, R. Zeng, F. Xing, C. Cheng, H. Qiu and C. Huang, *Nano Res.*, 2022, **15**, 6695–6704.
49 Y. Dong, D. Zhang, D. Li, H. Jia and W. Qin, *Sci. China Mater.*, 2023, **66**, 1249–1255.
50 D. An, J. Wang, J. Zhang, X. Zhai, Z. Kang, W. Fan, J. Yan, Y. Liu, L. Lu, C.-L. Jia, M. Wuttig, O. Cojocaru-Mirédin, S. Chen, W. Wang, G. J. Snyder and Y. Yu, *Energy Environ. Sci.*, 2021, **14**, 5469–5479.
51 Y.-J. Kim, L.-D. Zhao, M. G. Kanatzidis and D. N. Seidman, *ACS Appl. Mater. Interfaces*, 2017, **9**, 21791–21797.
52 M. Li, Y. Liu, Y. Zhang, C. Chang, T. Zhang, D. Yang, K. Xiao, J. Arbiol, M. Ibáñez and A. Cabot, *Chem. Eng. J.*, 2022, **433**, 133837.
53 Y. Gu, X. Liu, S. Huang, J. Guo, P. Bi, J. Shi, W. Zheng, Z. Wang and R. Xiong, *Ceram. Int.*, 2018, **44**, 21421–21427.
54 C. Nagarjuna, P. Dharmaiah, J.-H. Lee, K. B. Kim, G. Song, J. K. Lee and S.-J. Hong, *J. Alloys Compd.*, 2021, **881**, 160499.
55 Y. Zheng, Q. Zhang, X. Su, H. Xie, S. Shu, T. Chen, G. Tan, Y. Yan, X. Tang, C. Uher and G. J. Snyder, *Adv. Energy Mater.*, 2015, **5**, 1401391.
56 K. H. Lee, S.-i. Kim, J.-C. Lim, J. Y. Cho, H. Yang and H.-S. Kim, *Adv. Funct. Mater.*, 2022, **32**, 2203852.
57 D.-W. Liu, J.-F. Li, C. Chen and B.-P. Zhang, *J. Electron. Mater.*, 2011, **40**, 992–998.
58 S. Jo, S. H. Park, H. W. Ban, D. H. Gu, B.-S. Kim, J. H. Son, H.-K. Hong, Z. Lee, H.-S. Han, W. Jo, J. E. Lee and J. S. Son, *J. Alloys Compd.*, 2016, **689**, 899–907.
59 J. Yang, L. Xi, W. Qiu, L. Wu, X. Shi, L. Chen, J. Yang, W. Zhang, C. Uher and D. J. Singh, *npj Comput. Mater.*, 2016, **2**, 15015.
60 H.-s. Kim, K. H. Lee, J. Yoo, J. Youn, J. W. Roh, S.-i. Kim and S. W. Kim, *Materials*, 2017, **10**, 763.
61 C. Hu, K. Xia, C. Fu, X. Zhao and T. Zhu, *Energy Environ. Sci.*, 2022, **15**, 1406–1422.
62 J. He, S. N. Girard, J.-C. Zheng, L. Zhao, M. G. Kanatzidis and V. P. Dravid, *Adv. Mater.*, 2012, **24**, 4440–4444.
63 Z. Chen, X. Zhang and Y. Pei, *Adv. Mater.*, 2018, **30**, 1705617.
64 Z. Chen, Z. Jian, W. Li, Y. Chang, B. Ge, R. Hanus, J. Yang, Y. Chen, M. Huang, G. J. Snyder and Y. Pei, *Adv. Mater.*, 2017, **29**, 1606768.
65 H. S. Kim, S. I. Kim, K. H. Lee, S. W. Kim and G. J. Snyder, *Phys. Status Solidi B*, 2017, **254**, 1600103.
66 M. Gao and D. M. Rowe, *Meas. Sci. Technol.*, 2001, **12**, 1261.
67 J. Mao, Z. Liu, J. Zhou, H. Zhu, Q. Zhang, G. Chen and Z. Ren, *Adv. Phys.*, 2018, **67**, 69–147.
68 Q. Shi, J. Li, X. Zhao, Y. Chen, F. Zhang, Y. Zhong and R. Ang, *ACS Appl. Mater. Interfaces*, 2022, **14**, 49425–49445.
69 M. Maksymuk, B. Dzundza, O. Matkivsky, I. Horichok, R. Shneck and Z. Dashevsky, *J. Power Sources*, 2022, **530**, 231301.
70 B. Cai, H.-L. Zhuang, Q. Cao, H. Hu, J. Dong, Asfandiyar and J.-F. Li, *ACS Appl. Mater. Interfaces*, 2020, **12**, 16426–16435.
71 J. Li, Q. Tan, J.-F. Li, D.-W. Liu, F. Li, Z.-Y. Li, M. Zou and K. Wang, *Adv. Funct. Mater.*, 2013, **23**, 4317–4323.
72 Z. Guo, K. Song, Z. Yan, P. Sun, X. Tan, G. Wu, Q. Zhang, G.-Q. Liu, B. Yu and J. Jiang, *Chem. Eng. J.*, 2021, **426**, 131853.
73 C. Zhang, H. Ng, Z. Li, K. A. Khor and Q. Xiong, *ACS Appl. Mater. Interfaces*, 2017, **9**, 12501–12510.
74 Y. Pan, Y. Qiu, I. Witting, L. Zhang, C. Fu, J.-W. Li, Y. Huang, F.-H. Sun, J. He, G. J. Snyder, C. Felser and J.-F. Li, *Energy Environ. Sci.*, 2019, **12**, 624–630.
75 R. Deng, X. Su, Z. Zheng, W. Liu, Y. Yan, Q. Zhang, V. P. Dravid, C. Uher, M. G. Kanatzidis and X. Tang, *Sci. Adv.*, 2018, **4**, eaar5606.
76 Y. Zhang, X. Jia, H. Sun, B. Sun, B. Liu, H. Liu, L. Kong and H. Ma, *J Materiomics*, 2016, **2**, 316–323.
77 W. H. Shin, J. W. Roh, B. Ryu, H. J. Chang, H. S. Kim, S. Lee, W. S. Seo and K. Ahn, *ACS Appl. Mater. Interfaces*, 2018, **10**, 3689–3698.